Coexistence of triple nodal points, nodal links, and unusual flat bands in intermetallic APd$_3$ (A = Pb, Sn)

Kyo-Hoon Ahn,[1] Warren E. Pickett,[2,*] and Kwan-Woo Lee[1,3,†]

[1]*Department of Applied Physics, Graduate School, Korea University, Sejong 30019, Korea*
[2]*Department of Physics, University of California, Davis, California 95616, USA*
[3]*Division of Display and Semiconductor Physics, Korea University, Sejong 30019, Korea*

We investigate the electronic structure and several properties, and topological character, of the cubic time-reversal invariant intermetallic compounds PbPd$_3$ and SnPd$_3$ using density functional theory based methods. These compounds have a dispersionless band along the Γ-X line, forming the top of the Pd 4d bands and lying within a few meV of the Fermi level E_F. Effects of the flat band on transport and optical properties have been inspected by varying the doping concentration treated with the virtual crystal approximation for substitution on the Pb site. In the absence of spin-orbit coupling (SOC), we find triple nodal points and three-dimensional nodal loops, which are known to lead to surface bands and drumhead states, respectively, which we discuss for PbPd$_3$. SOC removes degeneracy in most of the zone, providing a topological index $Z_2 = 1$ on the $k_z = 0$ plane that indicates a topological character on that plane. The isovalent and isostructural compound SnPd$_3$ shows only minor differences in its electronic structures, so it is expected to display similar electronic, transport, and topological properties.

I. INTRODUCTION

For the last decade one of the most active issues in condensed matter physics is topological character of the electronic structure and the new properties that may arise. Various types of topological matters have been proposed and some have received experimental support. In addition to topological insulators, three-dimensional topological semimetals have attracted large interest due to their unusual boundary states [1], which may stimulate novel directions in electronics and spintronics separate from topological insulators. Recently, a novel triple point fermionic phase, having no high energy counterparts, has been also proposed in both nonsymmorphic [2] and symmorphic structures [3]. This phase, predicted along the symmetry line with threefold rotation and mirror (C_{3v}) symmetries in a few systems of WC-type or half-Heusler structures [4–7], is expected to have various unconventional properties and is experimentally observed in MoP [8].

The intermetallic palladium-lead phase diagram includes various compounds [9,10]. Among them, the so-called ideal zvyagintsevite compound PbPd$_3$ (cubic Cu$_3$Au structure) has been investigated as a catalyst for electrochemical oxygen reduction [11–13]. It has been known that its sister compounds can absorb a large amount of hydrogen [14,15], making them of interest as candidates for hydrogen storage or membrane separation.

Separately, flat bands in part or all of the Brillouin zone (BZ) have piqued interest for a variety of reasons. A weakly dispersive band leads to a peak in density of states (DOS), typically much stronger and perhaps narrower than structures arising from van Hove singularities. When a DOS peak is close to, or at, the Fermi level E_F, instabilities of the simple Fermi liquid states are encouraged; peaks can enhance a superconducting critical temperature or induce Stoner-type magnetic instability [16–18]. In PbPd$_3$ a remarkably flat band appears along the Γ-X lines, arising from a lack of $dd\delta$ hopping such as occurs in (cubic) perovskitelike systems [18,19]. Because of the limited phase space where the band is flat, it leads to two-dimensional-like step in the DOS (see below). It becomes of importance because it lies within a few meV of E_F, implying that transport, thermodynamic, and infrared properties will display unusual dependencies on temperature, doping, or other changes in the system (viz. strain).

The paper is organized as follows. Section II describes our calculational methods based on an *ab initio* approach. The electronic structure and topological characters of PbPd$_3$ are presented in Sec. III. Section IV discusses the effects of the unusual flat band on transport and optical properties. A brief comparison of electronic structures between PbPd$_3$ and SnPd$_3$ is addressed in Sec. V. Finally, Sec. VI provides a summary.

II. APPROACH

We have performed density functional theory calculations based on the exchange-correlation functional of the Perdew-Burke-Ernzerhof generalized gradient approximation (GGA) [20] with the all-electron full-potential code WIEN2K [21]. Since Pb is a heavy atom, spin-orbit coupling (SOC) is included in all calculations unless otherwise noted. Figure 1(a) shows the cubic Cu$_3$Au crystal structure (space group: $Pm\bar{3}m$, No. 221), with experimental lattice parameters of $a = 4.035$ Å for PbPd$_3$ [12,22] and $a = 3.971$ Å for SnPd$_3$ [23,24]. Both experimental
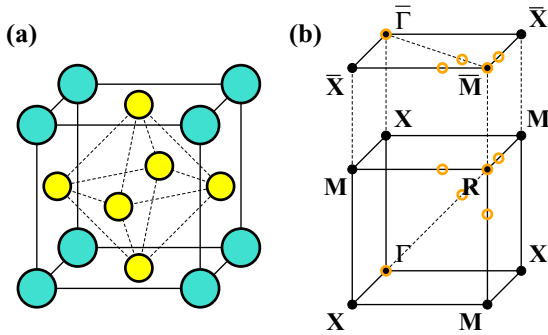
*pickett@physics.ucdavis.edu
†mckwan@korea.ac.kr

FIG. 1. (a) Cubic $L2_1$ crystal structure of $\mathcal{A}\mathrm{Pd}_3$, having a Pd_6 octahedron. (b) The bulk and (001) surface Brillouin zones (BZs) with high symmetry points. The unfilled circles denote positions of spinless triple nodal points, appearing in the range of -0.3 to 0.2 eV.

parameters are smaller by about 2% than our values optimized in GGA. Here our calculations were based on the experimental values, unless mentioned otherwise.

The topological properties were explored by the Wannier function approach. From the band structures obtained from WIEN2K, Wannier functions and the corresponding hopping amplitudes were generated using the WANNIER90 [25] and WIEN2WANNIER [26] programs. The surface spectral functions were calculated by the WANNIERTOOLS code [27].

The transport and optical properties were calculated by two extensions of WIEN2K. Based on the semiclassical Boltzmann transport theory with a constant scattering time approximation, the transport calculations were carried out with the BOLTZTRAP code [28]. Calculation of optical properties including SOC is available in the OPTICS [29]. Assuming an inverse scattering lifetime $\gamma = 10$ meV in the intraband contribution, the dielectric function $\epsilon(\omega)$, contributed by both intra- and interband excitations, was calculated. The electronic energy loss function is given by $-\mathrm{Im}[\epsilon^{-1}(\omega)]$.

In WIEN2K, the BZ was sampled by a very dense k mesh $40 \times 40 \times 40$ due to its sharp DOS structure near E_F. For a careful check of the position of the flat band, a high value of basis set cutoff $R_{\mathrm{mt}}K_{\mathrm{max}} = 9$ was used to determine the basis size with atomic radii of 2.5 bohrs for both ions.

III. ELECTRONIC AND TOPOLOGICAL CHARACTERS OF PbPd₃

A. Electronic structure of PbPd₃

The band structures of both GGA and GGA+SOC near E_F are shown in Figs. 2(a) and 2(b). In this energy regime, the bands have mostly Pb $6s$, $6p$ above E_F and Pd $5d$ character below. The corresponding density of states (DOS) with Pd $5d$ orbital-projected DOS is given in Fig. 2(c).

The band structure shows unusual characteristics relating to transport, thermodynamic, and topological properties. Most prominently, a very flat band of Pd $5d$ character appears along the Γ-X line only a few meV above E_F. The lack of dispersion reflects the lack of nearest neighbor (NN) Pd $dd\delta$ hopping. This characteristic appears commonly in cubic perovskite-related systems [19], but is unusual in intermetallic compounds. As indicated in Fig. 2(a), for the Γ-X line along the (100) direction,

the flat band has solely the d_{yz} orbital character of Pd2 $(\frac{1}{2}\frac{1}{2}0)$ and Pd3 $(\frac{1}{2}0\frac{1}{2})$ ions. Significantly, in PbPd₃ this flat band lies only 6 meV above E_F, thereby giving an effective Fermi energy for holes of $E_{F,h}^* = 6$ meV and corresponding Fermi temperature $T_{F,h}^* = 70$ K. As can be seen in Fig. 2(c), structure in the DOS is a 2D-like step discontinuity, and electron doping of only ~ 0.01 carrier/f.u. would be required to move E_F up to the band edge. Above the edge, the DOS is very small (semimetal-like) up to 0.2 eV.

Another aspect that we will follow is an occurrence of three-fold degeneracies along symmetry lines, which are becoming known as triple nodal points (TNPs). In the absence of SOC, as shown in Fig. 2(a), spinless TNPs $\Gamma_4^{\pm}$ appear at the Γ point. Along the Γ-R line, having the C_{3v} symmetry, the Γ_4^- band at 0.1 eV splits into a doublet Λ_3 of a positive effective mass and a singlet Λ_1 of a negative effective mass. The Γ_4^+ band slightly above E_F splits into a doublet Λ_3 and a singlet Λ_2, both with negative effective masses. As previously noted [2,3], the Λ_3 and Λ_1 crossing forms a TNP at $(0.39, 0.39, 0.39)\frac{2\pi}{a}$ at 0.15 eV along the Γ-R.

At the R point, a TNP of R_4^+ symmetry lies at -0.32 eV. This band splits into a doublet T_5 of a positive effective mass and a singlet T_2 along the R-M line, having C_{4v} symmetry. This doublet forms a TNP with the T_4 at $(\frac{1}{2}, \frac{1}{2}, 0.312)\frac{2\pi}{a}$ at 0.19 eV. The TNP along the C_{4v} symmetry line has not been discussed previously. One may expect surface states connecting these spinless TNPs in the absence of SOC. The surface states for PbPd₃ are discussed below.

In addition to TNPs, there is a nodal point at ~ 0.5 eV along the R-M line at $(\frac{1}{2}, \frac{1}{2}, 0.3983)\frac{2\pi}{a}$. Perpendicular to this line and along cubic directions, this double degeneracy *does not split*, forming the three interconnected topological nodal loops shown in Fig. 3(c). The three nodal loops lie on mutually perpendicular mirror planes. These R-centered links are similar to what was reported in the antiperovskite $\mathrm{Cu}_3\mathrm{PdN}$ [30].

To probe the origin and sensitivity to symmetry lowering of these TNPs, the cubic structure has been distorted, conserving the volume. Tetragonal distortion leads to breaking C_{3v} symmetry, thereby removing TNPs along the (111) direction. Both the C_{3v} and C_{4v} symmetries are broken by orthorhombic distortion, resulting in the vanishing of the TNPs along both the R-M line as well as along the $\langle 100 \rangle$ directions. See the Supplemental Material for additional information [31]. These TNPs are protected by the mirror plus threefold, or fourfold, rotational symmetries, respectively.

Comparison of the two band structures without and with SOC in Fig. 2 reveals several effects of SOC. SOC leads to anticrossing of several, but not all, crossing bands, as well as lowering the flat band toward E_F, from 15 to 5 meV. At the Γ point, two sixfold degenerate bands $\Gamma_4^{\pm}$ (including spin) split into doublet and quartet, resulting in a SOC gap of 0.3 eV due to a band inversion. Substantial impacts of SOC resulting in changes of surface states appear in the spinless TNPs along Γ-R-M lines near the R point at ~ 0.2 eV. As discussed by Zhu and co-workers [3], these TNPs are not protected in the cubic structure, when including SOC. Instead, SOC driven anticrossings at these TNPs lead to eight symmetry related fourfold degenerate Dirac points at ~ 0.2 eV along Γ-R, and six at ~ 0.15 eV along R-M. A similar behavior along a C_{6v}
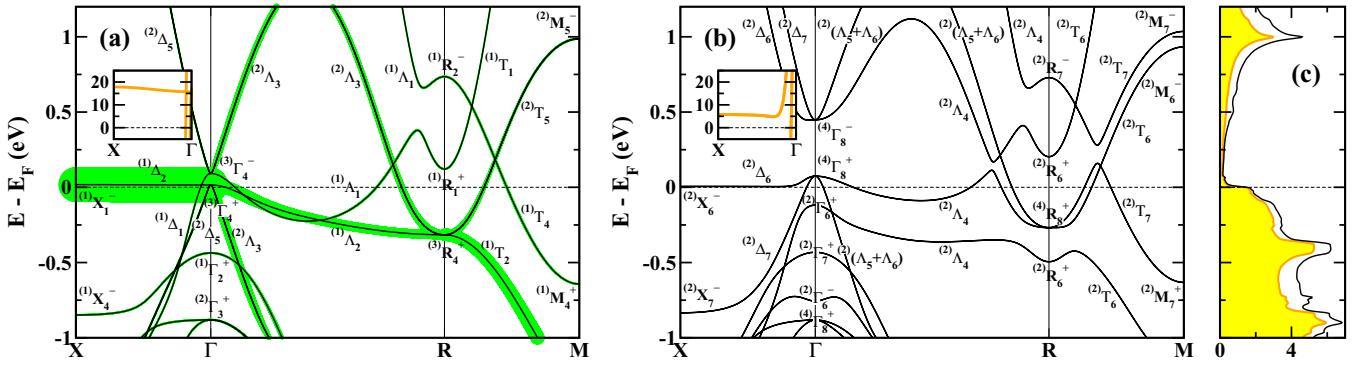
FIG. 2. Enlarged view of the (a) GGA and (b) GGA+SOC band structures labeled with with point group representations, along the X-Γ-R-M line around E_F, which is set to zero. The superscripts of the notations denote degeneracies of each band. At the high symmetry points, the $\pm$ symbols indicate parities of each band. The Γ-R line has a C_{3v} symmetry, while the other lines have C_{4v} symmetry. The insets show the flat band lying a few meV above E_F along the Γ-X line. The symmetry points of the band structures are given in Fig. 1(b). The X point is the zone boundary along the (100) direction. (c) The GGA+SOC density of states (DOS) of PbPd$_3$, in units of states/eV. The (yellow) shaded region corresponds to the orbital-resolved DOS of Pd $5d$ states. In (a), the d_{yz} characters of Pd2 ($\frac{1}{2}\frac{1}{2}0$) and Pd3 ($\frac{1}{2}0\frac{1}{2}$) ions are highlighted by thick (green) lines. Note that there is no contribution of Pd1 ($0\frac{1}{2}\frac{1}{2}$) ion to the flat band along this direction.

line was suggested in the layered hexagonal AlB_2-type metal diborides [32]. Thus the band structure is gapped at 0.2 eV except for the band emanating from R, strengthening the semimetal viewpoint of the near-E_F electronic structure of PbPd$_3$.

One result of this semimetallic band structure is delicate Fermi surfaces (FSs). Figure 3 displays the physical FSs (SOC included), consisting of three types. Narrow cylindrical open hole FSs lie along the (100) axes, intersecting at the zone center; these tubes are related to the flat band along Γ-X discussed above. An R-centered electron spheroid FS has a radius of $0.26(\frac{\pi}{a})$, containing 0.03 electrons per formula unit. Additionally, there are tiny elliptical hole pockets ("carrots") around this sphere along the {111} directions and tiny spheroids along the {100} directions.

Most results obtained for our optimized lattice parameter are very close to those for the experiment parameter presented above, as expected from the fact that the difference is small (less than 2%). There is however a distinction worth mentioning. For the optimized (larger) volume, the flat band is shifted to −5 meV relative to E_F. Thus modest pressure can be used to tune this band edge through the chemical potential for the stoichiometric composition. The position of the flat

band can also be tuned by either tetragonal or orthorhombic strain, with more information provided in the Supplemental Material [31].

B. Topological character of PbPd$_3$

Using a Wannier representation of the bands, we have carried out surface calculations based on the Green function approach [33] for a semi-infinite crystal. For PbPd$_3$, there are two possible (001) surface terminations, one containing both Pb and Pd atoms (Pb-Pd) and the other containing only Pd surface atoms (Pd$_2$). Figure 4 shows the surface spectral functions for the each termination, in both GGA and GGA+SOC. Around 0.2 eV above E_F the surface zone is gapped except around the $\bar{M}$ point, arising from the bulk bands around R that project onto $\bar{M}$.

In the absence of SOC, in Figs. 4(a) and 4(c) the Pd$_2$ termination shows a weakly dispersive surface band in both directions from $\bar{\Gamma}$. For the Pb-Pd terminated surface only surface resonances within the bulk bands appear along symmetry lines. Several surface states appear at the projections of TNPs both in the gap and inside the bulk states in both terminations. The positions of TNPs and their projections onto the surface BZ are
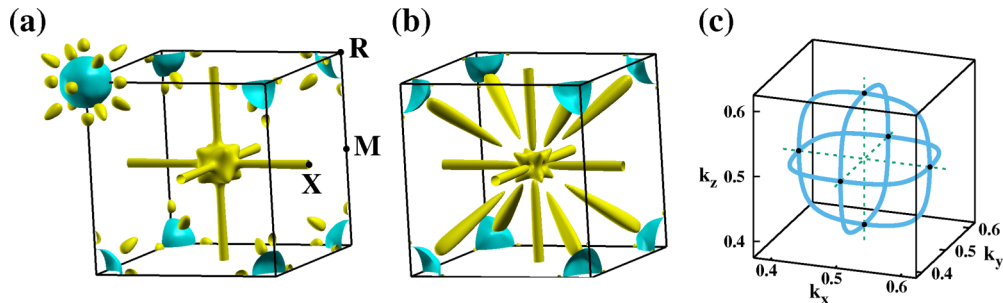

FIG. 3. GGA+SOC Fermi surfaces of (a) PbPd$_3$ and (b) SnPd$_3$. For PbPd$_3$, the R-centered sphere (blue) contains electrons, while the others (yellow) enclose holes. The 14 Dirac points in the PbPd$_3$ BZ lies along the R-Γ and R-M lines, coincidentally between the R-centered sphere and the carrotlike and spheroid hole pockets, see (a). In SnPd$_3$, large carrots appear along the (111) directions. (c) Nodal line isocontours connecting the Dirac points, denoted by black dots, at ∼0.5 eV along the M-R-M' line in GGA. The center of the fractional BZ is the R point.
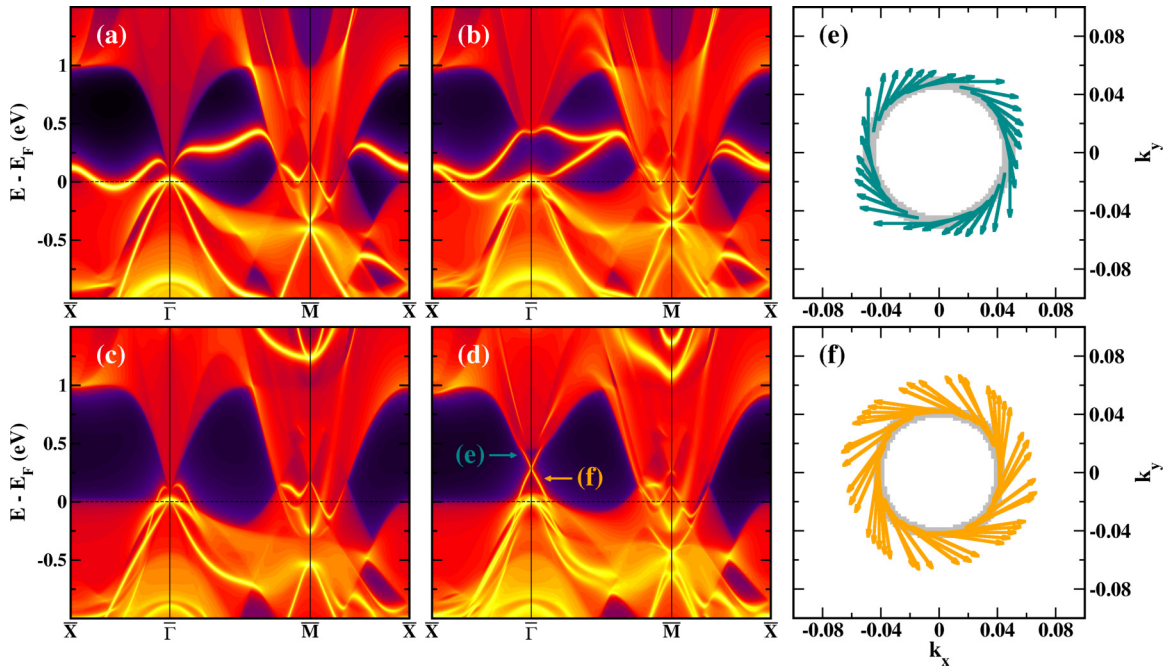
FIG. 4. The (001) surface spectral functions for (top) Pd_2 and (bottom) Pb-Pd terminations within (left) GGA and (middle) GGA+SOC. The reddish regions denote projections of bulk states. The right panels display the spin texture at the two-dimensional Dirac cone appearing in (d) at $\bar{\Gamma}$, having opposite helical texture in the (e) upper and (f) lower cones. The surface projected symmetry points are given in Fig. 1(b).

provided in Fig. 1(b). At $\bar{\Gamma}$ there is a surface band ~15 meV above E_F, corresponding to the TNP at Γ at 16 meV that projects onto $\bar{\Gamma}$. One of the TNPs (at 0.2 eV) along the R-M line projects onto $\bar{M}$, and any surface states that might be related are hardly evident, as it is within a strong background of projected bulk states around $\bar{M}$. The other two TNPs project onto the $\bar{M}$-$\bar{X}$ line, where a strong surface band appears within the gap at 0.1–0.3 eV, but only for the Pd_2 termination. This strong surface band is seen everywhere within the gap. Since it is missing for the PbPd terminated surface, its relation to TNPs is in doubt.

SOC is known to have strong consequences in nodal point and nodal loop materials. Inclusion of SOC leads to a large 0.4 eV gap just above E_F at the Γ point and all along the Γ-X line, hence a 0.4 eV gap at $\bar{\Gamma}$, resulting in qualitative changes in the surface spectrum. As shown in Fig. 4(b), in the Pd_2 termination the surface band in the absence of SOC becomes two surface bands, separated by a 0.4 eV gap around $\bar{\Gamma}$ point but connecting valence and conduction bands. These bands merge at $\bar{X}$ and also as they enter the bulk spectrum along the other two symmetry lines.

For Pb-Pd termination, where no surface bands around $\bar{\Gamma}$ appear within the gap in GGA, SOC produces a new occurrence, one that is very different from that of the Pd-Pd termination: a surface band Dirac point emerges at $\bar{\Gamma}$ at 0.25 eV above E_F from two linear bands joining valence to conduction bands, as shown in Fig. 4(d). This surface crossing is enabled by SOC opening a bulk gap at Γ. In the Pb-Pd termination, a 2D Dirac cone at the $\bar{\Gamma}$ point is a dominant feature. In Figs. 4(e) and 4(f) the spin textures are shown for cross sections of the cones just above, and just below, the Dirac point. The orientation of texture is in opposite helical direction in the upper and lower cones, reflecting the topological character of this point.

C. Fermi level spectral density

The surface Fermi level spectral density contours (the surface Fermi lines) are pictured in Fig. 5, presented analogously to Fig. 4. As expected from differences between the two
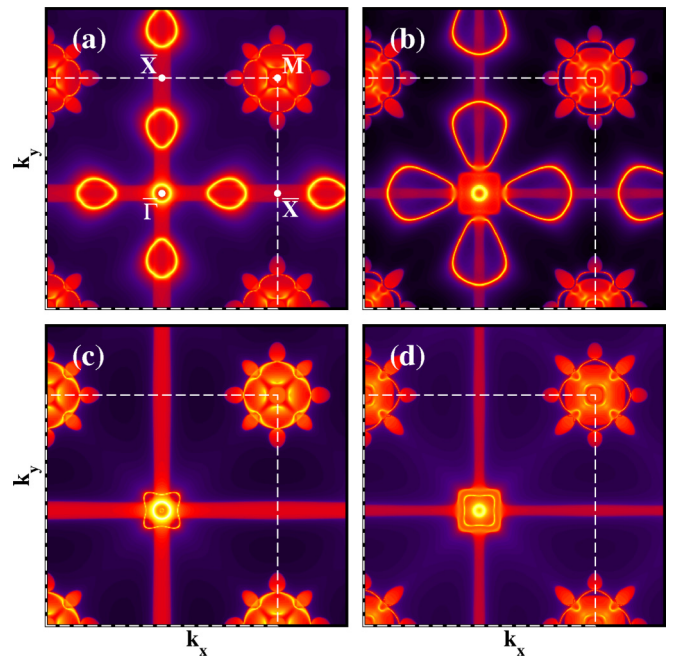

FIG. 5. Spectral densities of the surface Fermi contours of the surface states shown in Fig. 4, for (top) Pd_2 and (bottom) Pb-Pd terminations. The left panels are for GGA only, the right panels show results for GGA+SOC. The strong yellowish lines denote surface bands.
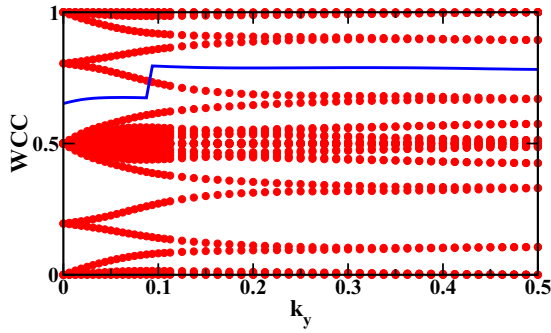
FIG. 6. Plot of the hybrid Wannier charge centers (WCCs) plot (red, thick lines) across half of the Brillouin zone in the $k_z = 0$ plane, showing an odd number of crossings between the charge center and largest gap among two adjacent WCCs. The gap function is designated by the blue (thin) line. The magnitude of the wave vector k_y in the horizontal axis is given in units of π/a.
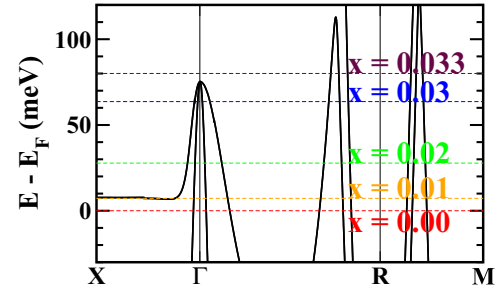

FIG. 7. Enlargement of the band structure in GGA+SOC, with horizontal lines denoting E_F as electron doping x is increased. The results are from the virtual crystal approximation applied to $(Pb_{1-x}Bi_x)Pd_3$. 1% doping puts E_F precisely on the flat band.

terminations in the surface spectrum, a clear distinction appears along the $\bar{\Gamma}$-$\bar{X}$ line, whereas features around $\bar{M}$ are nearly identical. For Pd_2 termination there are four symmetry related ovoid pockets along the axes, both without and with SOC. These are shown in Figs. 5(a) and 5(b), indicating that SOC substantially increases the area of these pockets (increases the density of the corresponding carriers). The bulk R point and its Fermi spheroid project onto the $\bar{M}$ point, and protrusions along axes and diagonals connected to this spheroid appear for both terminations. There is only small quantitative change with SOC. For higher resolution figures, see the Supplemental Material [31].

Calculations of the hybrid Wannier charge centers (WCCs) allow a "theoretical spectroscopy" of topological character in cases where the full zone is not gapped [34,35]. In this technique, the Bloch-to-Wannier transformation is applied only to one direction, and in cubic crystals there is only one choice of direction. These calculations were performed to establish topological character using the WANNIERTOOLS code [27]. In this method, the Z_2 number is calculated from the number of crossings of WCCs mod 2 by an arbitrary line in half of BZ, making use of time-reversal symmetry [34]. As a practical matter, instead of an arbitrary line, a line between two adjacent WCCs is chosen for numerical efficiency.

In PbPd$_3$, inclusion of SOC separates bands over most of the BZ, band crossings surviving only around the R point. Thus the electronic structure on the basal planes (viz. $k_z = 0$) can be considered as insulating subspaces, thus providing a well-defined Z_2 number that can be calculated using the WCC method. As shown in Fig. 6, there is an odd number of crossings of the largest gap with the charge centers, giving $Z_2 = 1$. This number is also obtained from parities of all occupied eigenstates at time-reversal invariant momenta in the $k_z = 0$ plane. The parities are given by -1 at Γ and $+1$ at X and M, for a product of -1, again indicating $Z_2 = 1$. Therefore this crystal is a topological insulator on the $k_z = 0$ plane.

D. Strain effects

We have considered tetragonal and orthorhombic distortions to investigate effects of strain. The Z_2 indices are well

defined in both $k_z = 0$ and π/c planes in both cases even for a small strain. Due primarily to a change of parity at Γ, the corresponding indices are 0;(0,0,0) for both cases, indicating a topologically trivial phase. However, in-gap surface states appear, similar to the topological crystalline insulating phase proposed in the tetragonal lattice [36] or the orthorhombic perovskite iridates [37]. For more information see the Supplemental Material [31].

Two sister compounds, semimetallic SnPt$_3$ and PbPt$_3$, are worthy of comment. In contrast to the Pd analogies with several TNPs above E_F, the valence bands are fully filled, so SOC leads to well separated bands around E_F throughout the BZ [38]. SnPt$_3$ has been proposed as a weak topological insulator [39], while PbPt$_3$, with its additional complexities, will be discussed elsewhere [38].

IV. ROLE OF THE FLAT BAND; ELECTRON DOPING

We have varied the electron concentration in $(Pb_{1-x}Bi_x)Pd_3$, which is experimentally accessible [22], to inspect the role of the flat band in transport and optical properties, using the virtual crystal approximation, for which this is an optimal application. We will focus on GGA+SOC results. There is negligible change in band structure, and Fig. 7 displays the rising of the Fermi level with added electrons. The flat band precisely lies at E_F for $x = 0.01$, and by $x = 0.02$ the intersecting cylinder FSs disappear. At $x = 0.033$, the hole pockets at the Γ point are filled. Since transport and optical properties are derived from the bands ε_k, its derivatives, and the Fermi level position [40], one may anticipate specific features related with the flat band in PbPd$_3$. These properties are surveyed in the following subsections.

A. Transport properties

The transport properties have been calculated based on quasiclassical Bloch-Boltzmann transport theory [40], assuming a constant scattering time τ approximation. Our results including SOC are pictured in Fig. 8. The Hall coefficient $R_H(T)$, given in Fig. 8(a), shows substantial variation with temperature even at these very low doping levels. At zero doping $x = 0$, it is net (from competing Fermi surfaces) electronlike in sign. With increasing T, $R_H(T)$ monotonically decreases, and just above 800 K crosses zero, where electron and hole contributions
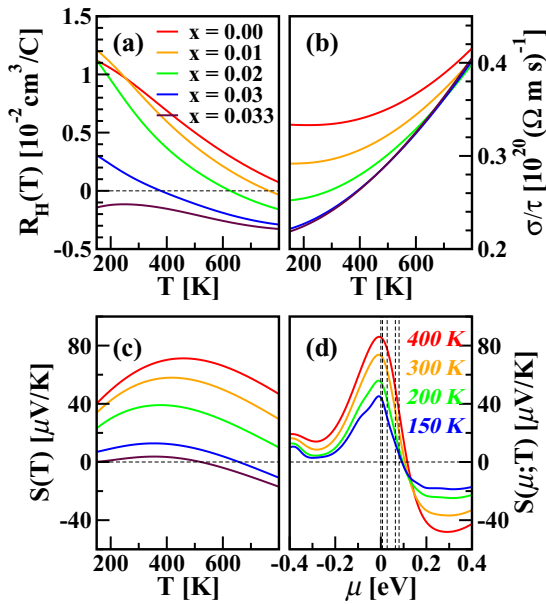
FIG. 8. As varying doped-electron concentration, temperature-dependent (a) Hall coefficients $R_H(T)$, (b) electronic conductivity σ over scattering time τ, and (c) Seebeck coefficients S for GGA+SOC in the range of 150–800 K. (d) Chemical potential μ-dependent Seebeck coefficients $S(\mu;T)$ for various temperatures in GGA+SOC. In (d), the vertical dashed lines indicate μ at each concentration, in the order of $x = 0$ to 0.033 from the left.

compensate. With increasing doping, $R_H(T)$ crosses zero at lower temperatures, e.g., for $x = 0.03$ exact compensation of holes and electrons occurs at 400 K. For $x = 0.033$, $R_H(T)$ is negative for the whole range of T, indicating dominance of hole carriers. Recall however that in a multiband system $R_H(T)$ has no simple relation to carrier densities [41].

Figure 8(b) shows the T-dependent conductivity over scattering time σ/τ. For a typical metal with large $N(E_F)$, σ/τ is proportional to $N(\mu)\langle v_F^2 \rangle$ [42] with insignificant T dependence. Here $N(\mu)$ and $\langle v_F^2 \rangle$ are the DOS at the chemical potential $\mu(T)$ and the thermal average of square of the Fermi velocity at $\mu(T)$, respectively. With structure in $N(E)$ around E_F, μ becomes T dependent. As T rises above 400 K ($x = 0$), σ/τ increases, by about 25% at 800 K, due to the sharp drop in $N(E)$ at 6 meV above E_F. As doping increases, the low temperature value drops and the temperature increase is enhanced as E_F moves upward with doping, through the DOS singularity and into the semimetal region.

Related variations are reflected in the Seebeck coefficient $S(T, x)$ [42], given by

$$S(T, x) = \frac{\pi^2}{3} \frac{k_B^2 T}{e} \left(\frac{d\ln\sigma(\varepsilon; T, x)}{d\varepsilon} \right)_\mu. \qquad (1)$$

As T increases, $S(T, x)$ increases up to about 300–500 K depending on x and then drops, as displayed in Fig. 8(c). For $x = 0.033$, $S(T, x)$ is very small, a condition that is poor for thermoelectric applications but can be favorable for other applications. Figure 8(d) presents a different viewpoint, plotting $S(\mu, T)$ versus μ at four values of T. At each temperature, the maximum occurs at $\mu(T) = 0$, followed by a steep drop through zero around $\mu = 0.1$ eV, before
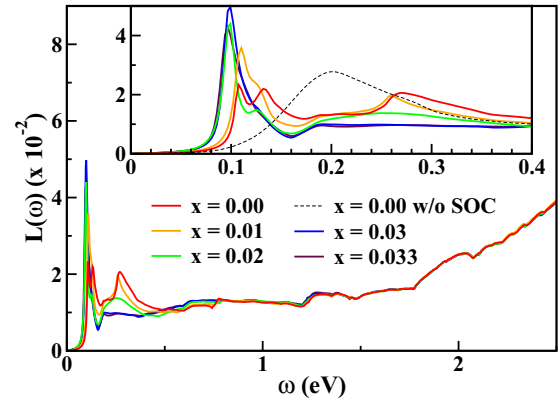

FIG. 9. Energy loss function $L(\omega)$ versus energy ω ($\hbar = 1$), for the various electron-doping levels. A scattering rate $\gamma = \hbar/\tau$ of 10 meV has been assumed, which primarily affects the widths of peaks but also determines the (small) intraband contribution. Inset: Enlarged plot below $\omega = 0.4$, showing the low energy plasmonic peak(s) clearly. For $x = 0$, the result without SOC is included to indicate the influence of SOC in the loss function.

leveling off beyond $\mu = 0.2$ eV. Measurement of the Seebeck coefficient, which is independent of scattering in the constant scattering time approximation, could be useful in determining the stoichiometry of $PbPd_3$ at the 1% level.

Although interesting features are visible in the x, μ, and T dependencies of the transport coefficients, there is nothing that is as striking as might have been expected given the anomalous $N(E)$ very near E_F. A contributing feature is that the FSs are small and varied in size and shape, and the Fermi velocities are small: on the crossed cylinders $v_F \sim 6.4 \times 10^6$ cm/s, compared to values 20 times larger for many intermetallic compounds.

B. Optical properties

The electron energy loss function $L(\omega)$, given in Fig. 9, was calculated as the imaginary part of the inverse dielectric function $\epsilon(\omega)$. The dielectric function includes both intra- and interband contributions. In the intraband part, containing the Drude term, an inverse scattering time τ is chosen from $\gamma = \hbar/\tau = 10$ meV.

The overall behavior of $L(\omega)$ is nonmonotonically dependent on an electron-doping level. $PbPd_3$ is a nearly transparent (semi)metal in the far infrared region $\omega < 75$ meV. At zero doping, the large loss peak at 0.2 eV when SOC is neglected is split by SOC, leaving a series of less pronounced subpeaks at 0.11, 0.14, and 0.27 eV. The plasmon peak around 0.1 eV is mainly due to excitation at the Γ point and has the strongest intensity at $x = 0.03$. The intensity and position of these peaks depends somewhat on the choice of γ.

V. THE Sn ANALOG

Isovalent and isostructural $SnPd_3$, with a 1.5% smaller lattice constant than $PbPd_3$, was also investigated. As expected, the band structure of $SnPd_3$, presented in Fig. 10(a), is very similar to that of $PbPd_3$, using GGA only. However, in $SnPd_3$ effects of SOC are not as substantial as in $PbPd_3$, since the
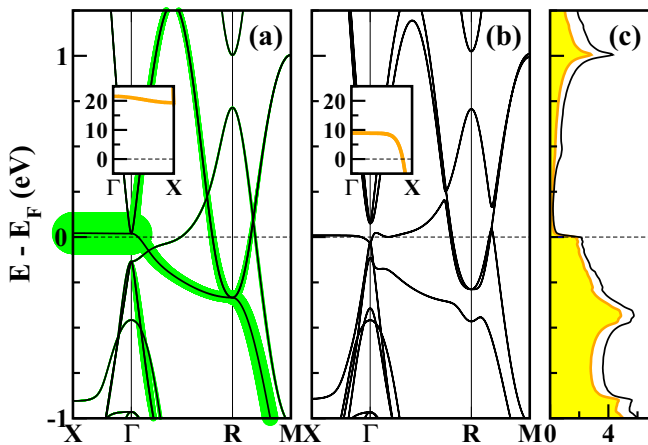
FIG. 10. The band structure and density of states of SnPd$_3$, as labeled, which can be compared with that of PbPd$_3$ in Fig. 2.

strength of SOC in Sn is weaker than in Pb. The GGA+SOC band structure and the corresponding DOS are displayed in Figs. 10(b) and 10(c). Compared to PbPd$_3$, there are two distinctions worth noting. First, the flat band, which is shifted downward by SOC, lies at 10 versus 6 meV for PbPd$_3$. Second, the bottom conduction band lies very close to, but above, E_F along the Γ-R. These two features result in change in fermiology of SnPd$_3$, shown in Fig. 3(b) beside that of PbPd$_3$. The radius of the pipelike FS is increased and irregular rod-shape FSs appears along the {111} directions.

VI. SUMMARY

Using various calculations based on *ab initio* approach and semiclassical Bloch-Boltzmann theory, we have investigated the peculiar electronic structure, topological characters, and some transport characteristics of intermetallic PbPd$_3$, which has a very flat band along the Γ-X line nearly coinciding with the Fermi level. In the absence of SOC, several triple points emerge near E_F along the C_{3v} and C_{4v} symmetry lines, leading to surface Dirac cones along the $\bar{\Gamma}$-$\bar{M}$ lines and Fermi arcs around the zone corner on the surface states. Nodal points along the M-R-M' line lead to three-dimensional nodal links that lie on mirror planes. SOC removes degeneracies in most of the zone, leading to a topological insulating phase on the $k_z = 0$ plane. We have furthermore inspected effects of the unusual dispersionless band on transport and optical properties by varying the doping level.

Although there are some distinctions due to difference in strength of SOC between Pb and Sn ions, most of the electronic structure characteristics of PbPd$_3$, including the flat band, are shared with isovalent and isostructural SnPd$_3$, suggesting it will display similar transport, optical, and topological properties.

[1] For a review, see N. P. Armitage, E. J. Mele, and A. Vishwanath, Weyl and Dirac semimetals in three-dimensional solids, Rev. Mod. Phys. **90**, 015001 (2018).

[2] B. Bradlyn, J. Cano, Z. Wang, M. G. Vergniory, C. Felser, R. J. Cava, and B. A. Bernevig, Beyond Dirac and Weyl fermions: Unconventional quasiparticles in conventional crystals, Science **353**, aaf5037 (2016).

[3] Z. Zhu, G. W. Winkler, Q. Wu, J. Li, and A. A. Soluyanov, Triple Point Topological Metals, Phys. Rev. X **6**, 031003 (2016).

[4] H. Weng, C. Fang, Z. Fang, and X. Dai, Topological semimetals with triply degenerate nodal points in θ-phase tantalum nitride, Phys. Rev. B **93**, 241202(R) (2016).

[5] H. Weng, C. Fang, Z. Fang, and X. Dai, Coexistence of Weyl fermion and massless triply degenerate nodal points, Phys. Rev. B **94**, 165201 (2016).

[6] H. Yang, J. Yu, S. S. P. Parkin, C. Felser, C.-X. Liu, and B. Yan, Prediction of Triple Point Fermions in Simple Half-Heusler Topological Insulators, Phys. Rev. Lett. **119**, 136401 (2017).

[7] J. Wang, X. Sui, W. Shi, J. Pan, S. Zhang, F. Liu, S.-H. Wei, Q. Yan, and B. Huang, Prediction of Ideal Topological Semimetals with Triply Degenerate Points in the NaCu$_3$Te$_2$ Family, Phys. Rev. Lett. **119**, 256402 (2017).

[8] B. Q. Lv, Z.-L. Feng, Q.-N. Xu, X. Gao, J.-Z. Ma, L.-Y. Kong, P. Richard, Y.-B. Huang, V. N. Strocov, C. Fang, H.-M. Weng, Y.-G. Shi, T. Qian, and H. Ding, Observation of three-component fermions in the topological semimetal molybdenum phosphide, Nature (London) **546**, 627 (2017).

[9] Ph. Durussel and P. Feschotte, The binary system Pb-Pd, J. Alloys Comput. **236**, 195 (1996).

[10] H. Okamoto, Pb-Pd (lead-palladium), J. Phase Equilib. **18**, 491 (1997).

[11] Y.-S. Kim and J.-M. Choi, X-ray diffractometric study on modification mechanism of matrixes for electrothermal AAS determination of volatile lead and bismuth, Bull. Korean Chem. Soc. **21**, 56 (2000).

[12] Z. Cui, H. Chen, M. Zhao, and F. J. DiSalvo, High-performance Pd$_3$Pb intermetallic catalyst for electrochemical oxygen reduction, Nano Lett. **16**, 2560 (2016).

[13] T. Gunji, S.-H. Noh, T. Tanabe, B. Han, C. Y. Nien, T. Ohsaka, and F. Matsumoto, Enhanced electrocatalytic activity of carbon-supported ordered intermetallic palladium lead (Pd$_3$Pb) nanoparticles toward electrooxidation of formic acid, Chem. Mater. **29**, 2906 (2017).

[14] X. Ke, G. J. Kramer, and O. M. Lovvik, The influence of electronic structure on hydrogen absorption in palladium alloys, J. Phys.: Condens. Matter **16**, 6267 (2004).

[15] H. Kohlmann, A. V. Skripov, A. V. Soloninin, and T. J. Udovic, The anti-perovksite type hydride InPd$_3$H$_{0.89}$, J. Solid State Chem. **183**, 2461 (2010).

[16] E. Dagotto, A. Nazarenko, and M. Boninsegni, Flat Quasiparticle Dispersion in the 2D t-J Model, Phys. Rev. Lett. **73**, 728 (1994).

[17] M. Imada and M. Kohno, Superconductivity from Flat Dispersion Designed in Doped Mott Insulators, Phys. Rev. Lett. **84**, 143 (2000).

[18] H. Rosner, R. Weht, M. D. Johannes, W. E. Pickett, and E. Tosatti, Superconductivity Near Ferromagnetism in $MgCNi_3$, Phys. Rev. Lett. **88**, 027001 (2001).

[19] K.-W. Lee and W. E. Pickett, Orbital-ordering driven structural distortion in metallic $SrCrO_3$, Phys. Rev. B **80**, 125133 (2009).

[20] J. P. Perdew, K. Burke, and M. Ernzerhof, Generalized Gradient Approximation Made Simple, Phys. Rev. Lett. **77**, 3865 (1996).

[21] K. Schwarz and P. Blaha, Solid state calculations using WIEN2k, Comput. Mater. Sci. **28**, 259 (2003).

[22] J. T. Szymanski, L. J. Cabri, and J. H. G. Laflamme, The crystal structure and calculated powder-diffraction, data for zvyagintsevite, Pd_3Pb, Can. Mineral. **35**, 773 (1997).

[23] J. R. Knight and D. W. Rhys, The systems palladium-indium and palladium-tin, J. Less-Common Met. **1**, 292 (1959).

[24] O. T. Woo, J. Rezek, and M. Schlesinger, X-ray diffraction analyses of liquid-phase sintered compounds of Pd_3Sn and Ni_3Sn, Mater. Sci. Eng. **18**, 163 (1975).

[25] A. A. Mostofi, J. R. Yates, Y.-S. Lee, I. Souza, D. Vanderbilt, and N. Marzari, wannier90: A tool for obtaining maximally-localised Wannier functions, Comput. Phys. Commun **178**, 685 (2008).

[26] J. Kuneš, R. Arita, P. Wissgotte, A. Toschie, H. Ikedaf, and K. Held, Wien2wannier: From linearized augmented plane waves to maximally localized Wannier functions, Comput. Phys. Commun. **181**, 1888 (2010).

[27] Q. S. Wu, S. N. Zhang, H.-F. Song, M. Troyer, and A. A. Soluyanov, Wannier tools: An open-source software package for novel topological materials, Comput. Phys. Commun. **224**, 405 (2018).

[28] G. K. H. Madsen and D. J. Singh, BoltzTraP. A code for calculating band-structure dependent quantities, Comput. Phys. Commun. **175**, 67 (2006).

[29] C. Ambrosch-Draxl and J. O. Sofo, Linear optical properties of solids within the full-potential linearized augmented planewave method, Comput. Phys. Commun. **175**, 1 (2006).

[30] R. Yu, H. Weng, Z. Fang, X. Dai, and X. Hu, Topological Node-Line Semimetal and Dirac Semimetal State in Antiperovskite Cu_3PdN, Phys. Rev. Lett. **115**, 036807 (2015).

[31] See Supplemental Material at http://link.aps.org/supplemental/10.1103/PhysRevB.98.035130 for the band structures and HWCCs of the distorted structures, the blowup surface spectral functions.

[32] X. Zhang, Z.-M. Yu, X.-L. Sheng, H. Y. Yang, and S. A. Yang, Coexistence of four-band nodal rings and triply degenerate nodal points in centrosymmetric metal diborides, Phys. Rev. B **95**, 235116 (2017).

[33] M. P. Lopez Sancho, J. M. Lopez Sancho, J. M. L. Sancho, and J. Rubio, Highly convergent schemes for the calculation of bulk and surface Green functions, J. Phys. F **15**, 851 (1985); M. P. Lopez Sancho, J. M. Lopez Sancho, and J. Rubio, Quick iterative scheme for the calculation of transfer matrices: application to Mo (100), *ibid.* **14**, 1205 (1984).

[34] A. A. Soluyanov and D. Vanderbilt, Computing topological invariants without inversion symmetry, Phys. Rev. B **83**, 235401 (2011).

[35] For a brief review, see D. Gresch, G. Autés, O. V. Yazyev, M. Troyer, D. Vanderbilt, B. A. Bernevig, and A. A. Soluyanov, Z2Pack: Numerical implementation of hybrid Wannier centers for identifying topological materials, Phys. Rev. B **95**, 075146 (2017).

[36] L. Fu, Topological Crystalline Insulators, Phys. Rev. Lett. **106**, 106802 (2011).

[37] Y. Chen, Y.-M. Lu, and H.-Y. Kee, Topological crystalline metal in orthorhombic perovskite iridates, Nat. Commun. **6**, 6593 (2015).

[38] K.-H. Ahn, W. E. Pickett, and K.-W. Lee (unpublished).

[39] M. Kim, C.-Z. Wang, and K.-M. Ho, Coexistence of type-II Dirac point and weak topological phase in Pt_3Sn, Phys. Rev. B **96**, 205107 (2017).

[40] P. B. Allen, W. E. Pickett, and H. Krakauer, Anisotropic normal-state transport properties predicted and analyzed for high-T_c oxide superconductors, Phys. Rev. B **37**, 7482 (1988).

[41] K.-H. Ahn, K.-W. Lee, and W. E. Pickett, Spin-orbit interaction driven collective electron-hole excitations in a noncentrosymmetric nodal loop Weyl semimetal, Phys. Rev. B **92**, 115149 (2015).

[42] D. J. Singh, Doping-dependent thermopower of PbTe from Boltzmann transport calculations, Phys. Rev. B **81**, 195217 (2010).